



Bulletin of the Mineral Research and Exploration

<http://bulletin.mta.gov.tr>



Evaluation of current earthquake activity on the Ganos Fault: MONGAN network test analysis

Eşref YALÇINKAYA^{a*}, Marco BOHNHOFF^{b,c}, Ethem GÖRGÜN^a, Hakan ALP^a, Stephan BENTZ^b, Ali PINAR^d, Fatih ALVER^e, Ömer KILIÇARSLAN^c, Burçin Didem TAMTAŞ^a and Burçak GÖRGÜN^a

^aIstanbul University-Cerrahpaşa, Faculty of Engineering, Department of Geophysical Engineering, İstanbul, Türkiye

^bGFZ German Research Center for Geosciences, Potsdam, Germany

^cFree University of Berlin, Institute of Geological Sciences, Berlin, Germany

^dBoğaziçi University, Kandilli Observatory and Earthquake Research Institute, İstanbul, Türkiye

^eMinistry of Interior Disaster and Emergency Management Presidency, Ankara, Türkiye

Research Article

Keywords:

Ganos Fault,
Microearthquake, Fault
Zone Waves, Moment
Tensor Analysis.

ABSTRACT

The Monitoring of the Ganos Fault data presents significant opportunities and challenges for earthquake detection, location and magnitude calculations, source mechanism solutions, and discovery of fault zone waves. This study indicates mostly of preliminary data analysis and seismological evaluations. While narrow distance aperture installation has an opportunity to detect microearthquakes, it also causes significant difficulties in determining the source parameters of micro-earthquakes. Extracting microearthquakes from continuous data shows that special strategies need to be used. MONGAN data revealed the presence of many earthquakes with magnitude $M < 1.0$ in the study region. These earthquakes are mostly out of network earthquakes and it is very difficult to obtain reliable solutions due to the insufficient azimuthal distribution of the stations. It is obvious that different network techniques and wave particle motion analyzes are contributed to the location and source parameters. Although the fault zone structure consists of two different lithologies that make significant differences in seismic wave phase arrival times and wave amplitudes, we observe fault zone head waves on both sides along the Ganos fault. Moment tensor analyzes depict that reliable source mechanism solutions can be obtained using a small number of station records.

Received Date: 28.10.2021

Accepted Date: 05.04.2022

1. Introduction

The segment of the North Anatolian Fault Zone (NAFZ) within Marmara Sea (the section between the 1999 İzmit and 1912 Mürefte earthquake ruptures) is one of the best-known seismic gaps in the world (Figure 1). The westward migration of earthquakes along the NAFZ in the last century arrived in the Marmara Sea after the 1999 İzmit and Düzce earthquakes (Stein et al., 1997). Further west of the

fault, the Ganos Fault segment was broken by the 1912 $M_w=7.4$ Şarköy/Mürefte earthquake (Aksoy et al., 2010). The last known major earthquake along the Marmara Fault is the 1766 earthquake ($M_w 7.2$) and it has been characterized as an expired seismic cycle since approximately 250 years have passed (Bohnhoff et al., 2016; Bulut et al., 2019). In fact, the main Marmara fault is not a single segment consisting of several parts with different dynamic characteristics. It is claimed that the Tekirdağ segment in the west was

Citation Info: Yalçinkaya, E., Bonhoff, M., Görgün, E., Alp, H., Bentz, S., Pınar, A., Alver, F., Kılıçarslan, Ö., Tamtaş, B. D., Görgün, B. 2023. Evaluation of current earthquake activity on the Ganos Fault: MONGAN network test analysis. Bulletin of the Mineral Research and Exploration 170, 99-116. <https://doi.org/10.19111/bulletinofmre.1138208>

*Corresponding author: Eşref YALÇINKAYA, eyalcin@iuc.edu.tr

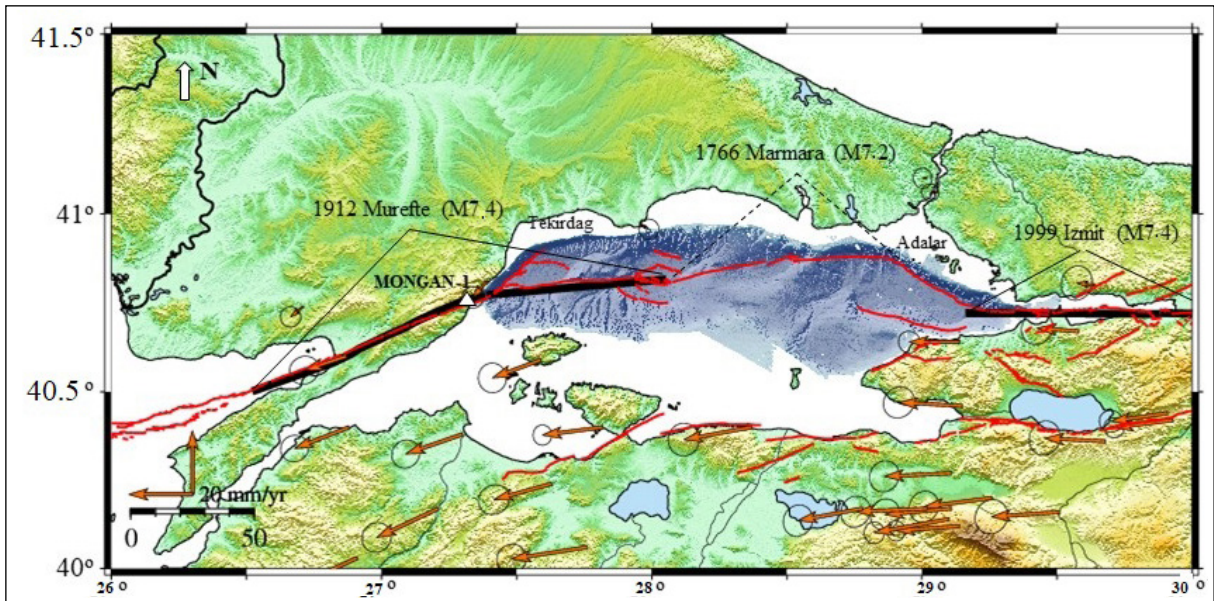


Figure 1- Main structural features of the study region and its surroundings. Red lines represent fault map (Armijo et al., 2005), arrows represent GPS vectors (McClusky et al., 2000), and thick black lines represent 1912 Mw7.4 Şarköy/Mürefte and 1999 İzmit earthquake ruptures. The MONGAN seismic network stations (MONGAN-1, white triangle) are enlarged in Figure 2.

broken by the 1912 earthquake (Armijo et al., 2005; Uçarkuş et al., 2011). The parts of Central Marmara and Princes Islands are the segments that are expected to be ruptured (Bohnhoff et al., 2013; Ergintav et al., 2014). While the Tekirdağ segment has intense seismicity and shows partly creep (Schmittbuhl et al., 2016; Bohnhoff et al., 2017; Uchida et al., 2019), the on-shore segment of the Ganos Fault together with the Saros Bay extension is an aseismic (non-earthquake-producing) and fully locked (Aksoy, 2021). Similarly, the Central Marmara segment exhibits an aseismic-locked feature (Bohnhoff et al., 2013; Lange et al., 2019), while the Princes Islands segment has high seismicity (Wollin et al., 2018). It is extremely important to investigate these multi-part and dissimilar seismic features of the main Marmara Fault in order to predict the real seismic hazard in the region.

One of the most important data in understanding the behavior of fault segments is to reveal different stress states by following the detailed geodetic and seismological features on the fault. However, this kind of detailed analyzes of the segments in the Marmara Sea is only possible with the sea floor observations close to the fault. In recent years, prominent studies focused on this subject are ocean bottom seismometer (OBS) (Özalaybey, 2010; Yamamoto et al., 2017)

and seafloor geodetic measurement networks (Sakic et al., 2016; Yamamoto et al., 2019). The number of microearthquakes recorded with OBS observation stations is approximately 5 times than obtained from conventional land observation networks (Yamamoto et al., 2022).

Revealing the velocity distribution of the opposite blocks and the crushed zone in a fault structure is crucial for many seismological analyzes and fracture mechanics. The velocity contrast between the fault blocks affects the progression and velocity of a rupture during an earthquake (Andrews and Ben-Zion, 1997). In addition, it is effective in terms of the estimation of earthquake location and rupture mechanisms (McGuire and Ben-Zion, 2005). In recent years, dense seismic networks along fault zones have allowed seismologists to verify the presence of fault zone head waves (FZHW) and fault zone trapped waves (FZTW) (Li and Leary, 1990; Ben-Zion and Malin, 1991).

An earthquake monitoring network consisting of 40 stations was established on-shore segment of the Ganos Fault (MONGAN- MONitoring of the GANos Network) in 2018 (Figure 2). The project was supported by the bilateral cooperation of the Scientific and Technological Research Council of Türkiye

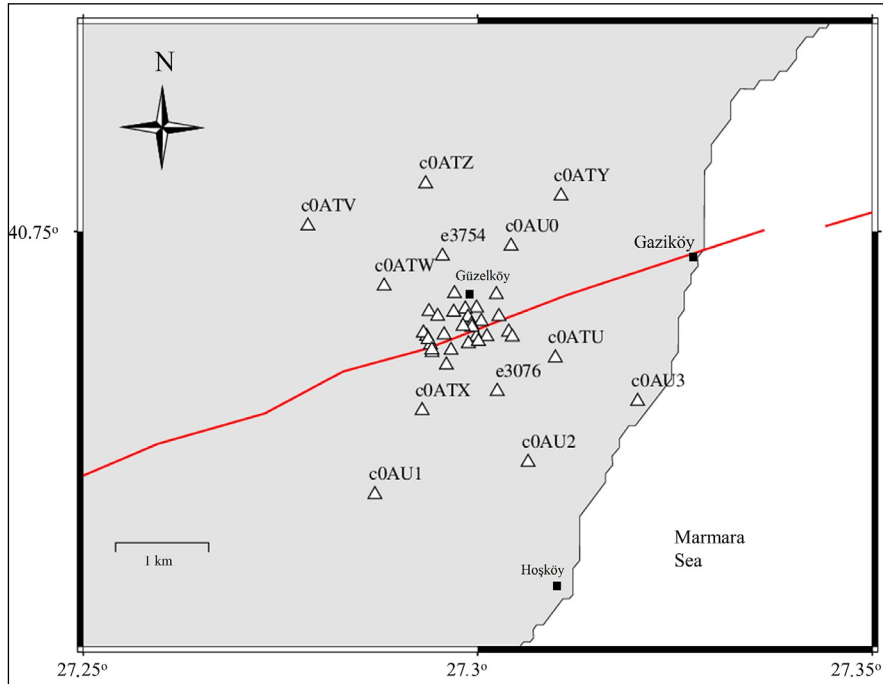


Figure 2- Station locations of MONGAN seismic network (MONGAN-1, triangles) along the Ganos Fault (red line). In order to avoid confusion, only the codes of external stations are given.

(TÜBİTAK) and the German Ministry of Education and Research (BMBF). The aim of the network is to observe a possible micro-seismic activity along the Ganos Fault where exhibits aseismic-locked behavior according to the data obtained from the national seismic networks (Kandilli Observatory and Earthquake Research Institute (KOERI) and the Disaster and Emergency Management Presidency (AFAD) and to image the bimaterial fault structure by analyzing fault zone waves. The seismic network is operated in two stages, in the first stage the stations are operated at the eastern end of the fault (MONGAN-1), in a narrow area for 2 years (Figure 2). In the second stage, the stations are shifted to the western part of the fault (MONGAN-2) and expanded to a wider area for approximately one year (Yalçinkaya et al., 2022). Two different types of sensors (Mark 1Hz L4C and Geophone 4.5Hz) and two different types of recorders (EarthData EDL PR6-24 and DATA-CUBE3) are used at the stations. In the first conjugate article, the characteristics of the seismic network, data collection and data quality were discussed (Yalçinkaya et al., 2022). In this second article, our primary aim is to compose initial tests of seismological analyzes using MONGAN-1 network data. We can list the

general characteristics of earthquakes recorded by the network as follows: They consist of mostly small or microearthquakes, they are also recorded at the stations located on the opposite fault blocks and directly fault zone which have different velocity structures. Lastly, they have mostly not good azimuthal station coverage for reliable location estimation. This study includes preliminary analyzes on the detection of earthquakes recorded by the network, magnitude and location estimation, the discovery of FZHW, and source mechanism solutions for small earthquakes.

2. Earthquake Detection

The process of detecting possible earthquakes from the continuous data recorded within the MONGAN network can be done in two ways, automatic and manual. Manual scanning of data is a very tedious and time-consuming process. Effective use of automatic detection is a priority in order to reduce the workload as much as possible and to use time efficiently. For this purpose, the first 3 months of the collected data were used to test the effectiveness of automatic detection. First, the continuous data were scanned with automatic detection, and then it was manually controlled for the

events missed or incorrectly detected. In the automatic process, the Short Term Average/Long Term Average (STA/LTA) method, which is one of the most basic applications, is used (Allen, 1978).

The parameters used in the STA/LTA method are tested many times in this study and the parameters that are decided to be the most successful ones are presented in Table 1. Generally, the STA is selected 1-2 seconds for regional events, while it can be reduced to 0.3-0.5 seconds for local events. The LTA can be tried starting from 60 seconds up to 30 seconds for local events. The STA/LTA triggering ratio, on the other hand, can be used around 3-4s for small earthquakes at stations with low-noise levels. As seen in Table 1, the automatic detection process starts with a band-pass filter in the range of 2-20 Hz. STA, LTA, and triggering ratio were determined as 0.3 s, 30 s, and 5, respectively. If triggering is provided at least 7 stations in the entire network, it is listed as an event. An event is cut from the continuous data for 180 seconds and stored as a separate file. These parameters may vary depending on the noise levels in the recordings and the number of operating stations at that time. In the second stage, an operator visually scans the data in 30-60 minute windows, using filters in different frequency bands, to delete the incorrectly determined events from the list and add the missed events to the list.

Table 1- Parameter values used in the STA/LTA method within condet subroutine used in the SEISAN (Havskov and Ottemoller, 1999) software.

Parameters	Values
Filter	2-20 Hz
STA time length	0.3 s
LTA time length	30 s
Triggering ratio (STA/LTA)	5
Triggering length (at least)	1 s
Triggering length (at least)	10 s
Number of triggered stations (at least)	7
Time length before triggering	30 s
Cut-off window length	180 s

Table 2- The number of events obtained as a result of automatic detection and manual control of the data collected in the first three months of the seismic network.

Dates of Event	Automatic detection	Manuel deleted	Manuel added	Ratio of difference	Exact number of events
01-31 October 2017	592	203	69	46%	458
01-30 November 2017	403	22	172	48%	575
01-31 December 2017	477	131	84	45%	417

Table 2 shows the comparison of automatic detection and manual control results for the first three months of the data. In general, it is seen that there are 40-50% of differences between automatic detection and manual control. Some of them are in the form of adding events that the automatic method could not detect, while the other part is in the form of deleting events due to false triggering. The high difference between automatic and manual detection indicates that the automatic method is not succeeded adequately. One of the main reasons for this is that the target earthquakes are too small. Microearthquakes generally remain in environmental noise and STA/LTA ratios are not successful enough to determine them. Testing different filters and viewing many station records simultaneously on the screen during manual control only made it possible to detect these earthquakes. Figure 3 displays two earthquakes discovered by automatic detection and manual control by using different filters, respectively. It may be possible to design the STA/LTA operator with the appropriate parameters for both earthquakes, but this time the number of false detection is highly increased. For more successful detection, it is aimed to use different automatic detection methods such as cross-correlation of waveforms in the next future of this study (Gibbons and Ringdal, 2006; Yoon et al., 2015; Bentz et al., 2019).

3. Phase and Amplitude Readings

In order to make the location and magnitude calculations of the selected earthquakes, the arrival times and amplitude values of the P and S wave phases are needed from the seismograms. While these readings can be made with high precision in data with a high signal-to-noise ratio, the error in the readings increases as signal-to-noise ratio decreases. Although automatic phase reading methods developed in recent years have produced very successful results, manual readings remain valid in terms of precision, especially

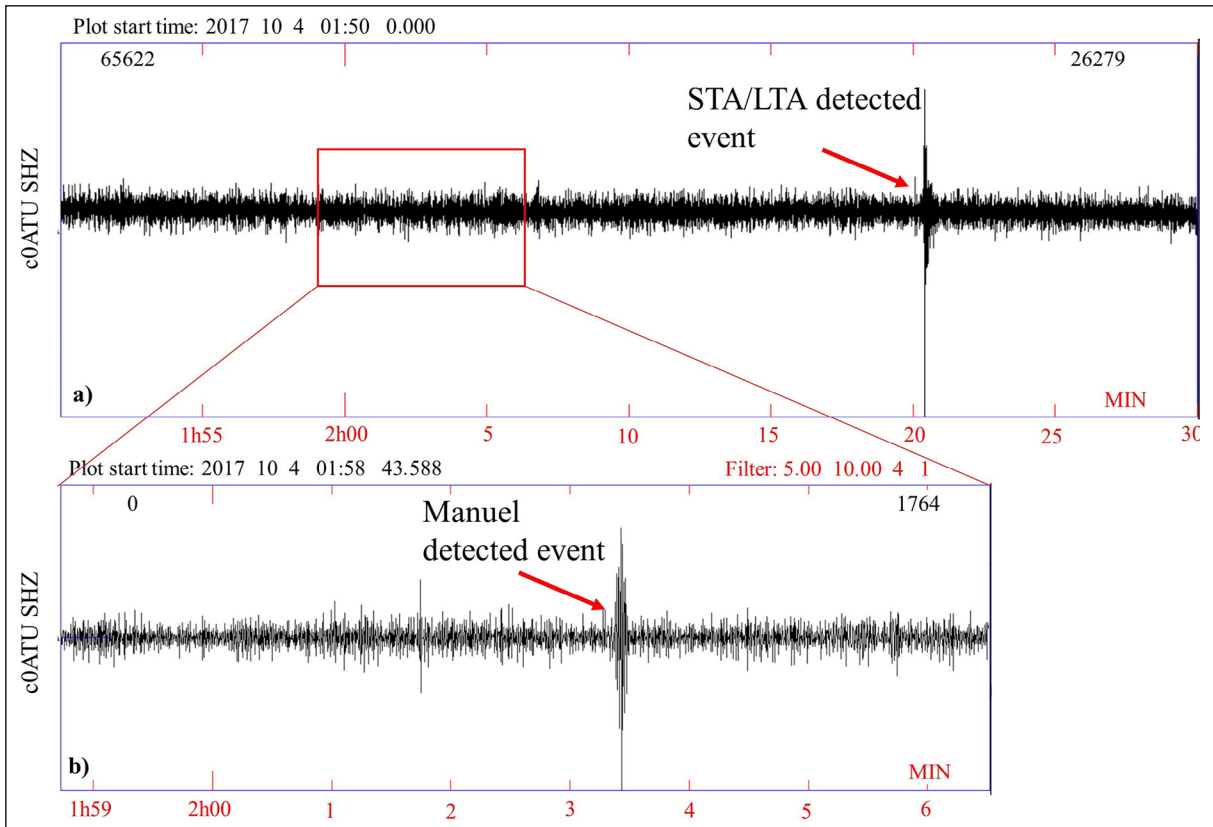


Figure 3- a) Discovered by automatic detection at the c0ATU station vertical component seismogram and b) manually detected a second event using a 5-10 Hz range filter within the red marked area of the same recording.

in cases where the signal-to-noise ratio is low and the waveforms between stations do not show many similarities.

In this study, phase and amplitude readings are done manually on unfiltered-raw data as much as possible. However, some readings can be made using different bandpass filters (e.g. 2-20 Hz, 5-30 Hz), especially in small earthquakes with the low signal-to-noise ratio. It should be noted that each filtering process creates some shifts in phase times and decreases in wave amplitudes. For these reasons, the selected filters are not distorted the general structure of the signal as much as possible. Very small apertures between seismic stations in the MONGAN-1 network require very high precision phase readings. Considering that the longest distance between stations is approximately 4 km, for a planar wave with a velocity of 6 km/s, the time difference occurs at these stations only 0.7 s. It should not be forgotten that this difference is much less at the near-vertical upcoming angles to the stations in close earthquakes.

Another important point in seismic phase reading is to distinguish different wave phases. The availability of different phases, as long as they are determined correctly, increases the accuracy of earthquake locations. These phases are the marking of the arrival times as Pn and Sn phases refracted from Moho, PS, SP phases transformed at the sediment-bedrock boundary, and the crustal Pg and Sg phases come directly to the receiver. Depending on the source-receiver geometry, it is not always possible to observe these phases in the seismograms. In some cases, these phases can be mixed with each other and may cause incorrect location solutions. Figure 4 shows sample phase markings for a three-component seismogram.

The local magnitude (M_L) scale is preferred in the magnitude calculation since local and small earthquakes are generally targeted in this study. First, the seismograms are simulated to a Wood-Anderson-type instrument using response functions and then displacement waveforms are calculated. As mentioned in Yalçinkaya et al. (2022), wave amplitudes clearly

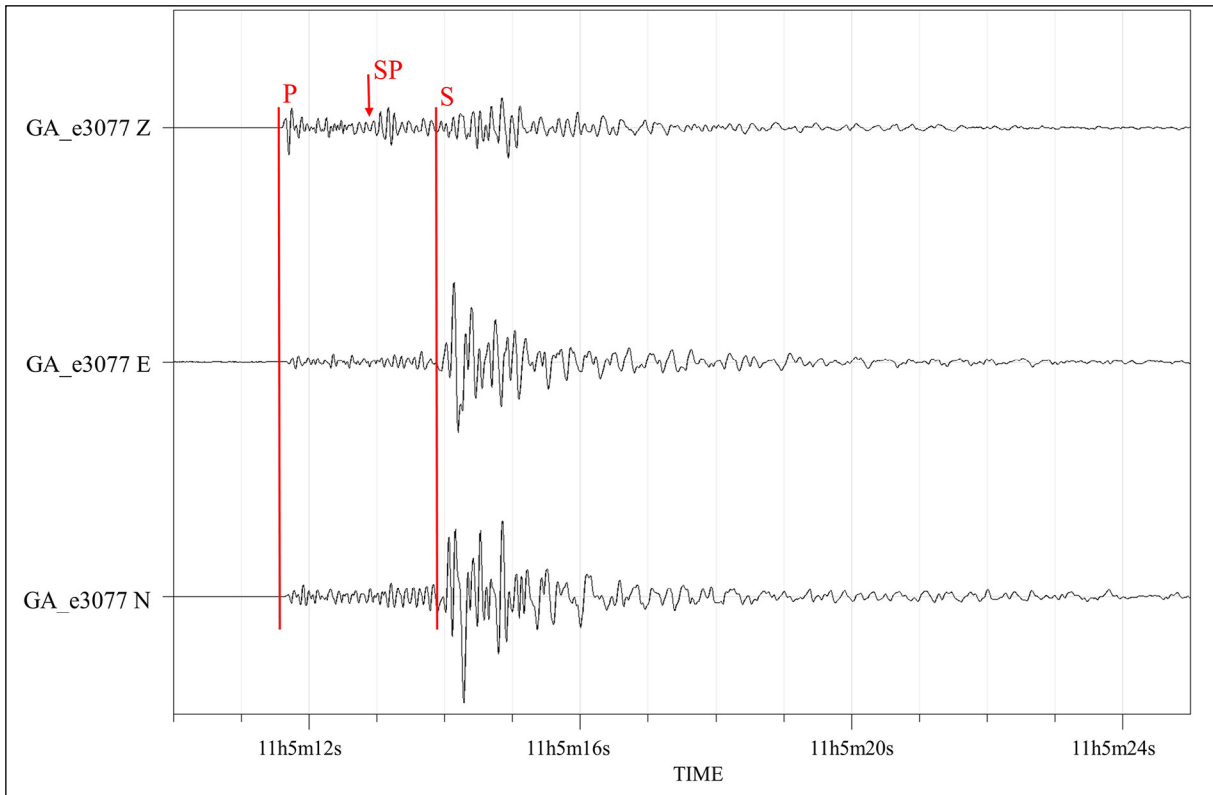


Figure 4- Three component earthquake seismogram and marking of P, S, and SP phases.

have near-surface soil effects, since the stations have different site properties. In order to minimize these effects, it is preferred to read the S wave amplitudes from the vertical component records in the M_L magnitude calculation (Equation 1) (Havskov and Ottemoller, 2010).

4. Location and Magnitude Calculations

The hypocenter algorithm (Lienert and Havskov, 1995) included in the SEISAN software (Havskov and Ottemoller, 1999) is used for location and magnitude calculations. In the first stage, 344 earthquakes that occurred between October 1 and November 30, 2017 are used as a test study. Different velocity models are tested in the analyses. In order to compare with KOERI solutions, which have a denser network in the region, Kalafat et al. (1987) velocity model is preferred.

The used equation for M_L ;

$$M_L = \log A + 1.0 \cdot \log R + 0,00167 \cdot R - 1,58 \quad (1)$$

In this equation, A : amplitude of S wave (mm) and R : distance of source (km). Regression coefficients

defined in Equation 1 are taken from Kılıç et al. (2016) which are obtained for earthquakes in Türkiye.

The earthquakes recorded by the MONGAN network and made solutions in this study are evaluated under three groups:

- i. Earthquakes detected and located by the national network
- ii. Earthquakes not located by the national network, but detected in both MONGAN and national network records
- iii. Earthquakes were detected only by the MONGAN network

The epicenter distribution of the located events (within the first 100 km radius) is shown in Figure 5. The minimum number of stations used in the locations is 19. Root mean error (RMS) values are generally below 0.3, but azimuthal gaps can reach up to 350 degrees, especially in the third group earthquakes. Calculated M_L magnitudes range from -0.7 to 4.3.

The first group of data contains earthquakes recorded by MONGAN, AFAD and/or KOERI stations, and also location-magnitude calculations done by these national agencies. The magnitudes for the first group of earthquakes are generally $M_L > 0.5$. The inclusion of MONGAN and national network stations together in the solution gives more reliable locations since they have a less azimuthal gap and more phase readings (Figure 5 yellow circles). The second group of earthquakes consists of events first discovered in the MONGAN network records and then included a limited number of national network station recordings (usually 1-5 stations) in the vicinity. These locations are shown in Figure 5 as red circles.

Their magnitudes are mostly $M_L < 1.0$ and their location accuracy which varies depending on the used station distribution is less reliable. Our third group of earthquakes represents events recorded only by MONGAN network stations (Figure 5 blue circles). These seismograms have relatively low signal-to-noise ratios. We use a different type of filters for their phase readings. Moreover, generally, they have very high azimuthal gaps. It is difficult to distinguish seismic phases due to the effects of the bimaterial fault zone properties. The magnitudes of these earthquakes are mostly below $M_L < 0.5$ and even negative values.

The epicenter and magnitude comparisons of the earthquakes for the first group of data, which are listed

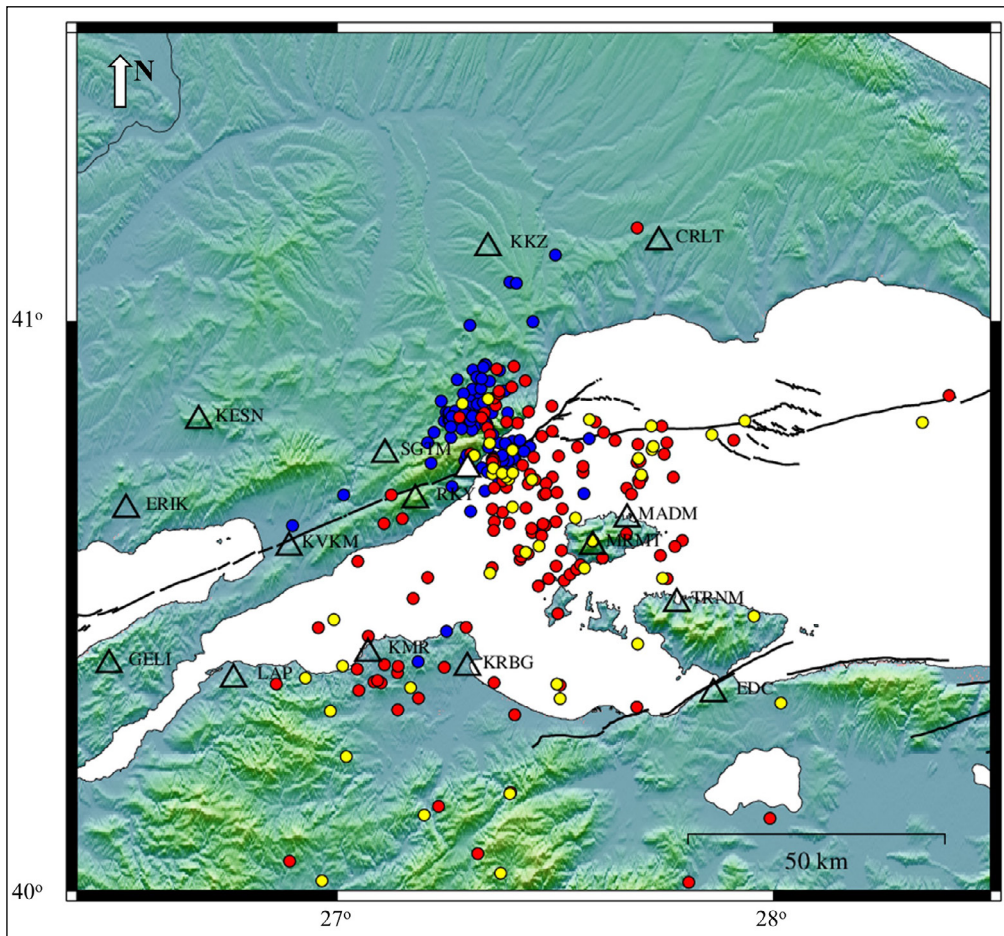


Figure 5- Location map of earthquakes analyzed in this study. The blank and white-filled triangles show the national network and the Ganos Fault monitoring network (MONGAN-1) stations used in the locations, respectively. Yellow circles represent earthquakes that are relocated by using the national network and MONGAN-1 network stations together. Red circles display earthquakes that are located by using the national network and MONGAN-1 network stations together in this study. These locations are not included in the national catalogs. Blue circles represent earthquakes located only by MONGAN-1 network. These events are also not listed in the national catalogs.

in the national catalog as well, are shown in Figures 6a and 6b, respectively. As can be seen, the epicenter solutions obtained in this study and listed in the KOERI catalog are very close to each other except for a few earthquakes. The magnitudes obtained in this study are slightly smaller than the KOERI catalog. Especially, these differences are obvious in small-magnitude earthquakes. The main factor causing this difference may be using the vertical seismogram amplitudes in the magnitude calculation. Amplitude readings are used from vertical components due to local site effects, especially at stations located on soft soils.

The magnitude-distance comparison of the earthquakes for the three groups is given in Figure 7. As seen in the figure, the main contribution of the MONGAN-1 network to the determination of the seismicity in the region occurs at distances of less than about 100 km and in events with magnitude $M_L < 1.0$ (Figure 7 red and blue circles). The earthquakes located by the national networks (excluding OBS) can detect in the region are generally observed as $M_L > 1.0$ earthquakes (Figure 7 black circles).

The third group of earthquakes based only on MONGAN-1 network recordings have high location errors. The biggest factor for this case is that MONGAN-1 stations do not provide good azimuthal coverage for most events, furthermore, azimuthal gaps are so high. The short distances between stations mean that in most earthquakes that occur outside the network, the network acts as a point receiver.

Another finding that is thought to cause errors in the locations is that the wave phases arrive at the stations located in the north of the fault systematically earlier than the stations located in the south. It is known that the Ganos Fault separates two different geological units in the region (Okay et al., 2010). The block in the north of the fault consists of Eocene-aged harder rocks, while the block in the south consists of Miocene-aged softer units. Therefore, it is normal for these units to have different seismic velocities, and for the northern block to have a higher wave propagation velocity than the southern block. In the sample seismogram examined, early wave phase arrivals to the stations in the northern block are clearly seen, although the source distance is the same at both station

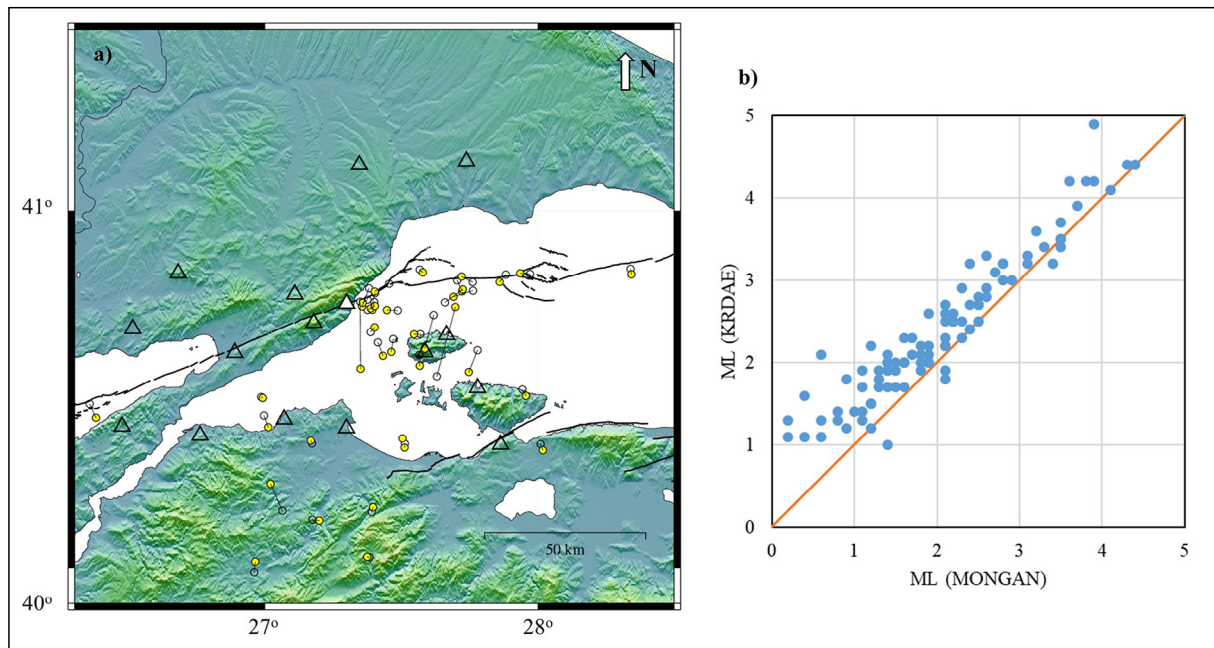


Figure 6- a) Comparison of earthquake locations (blank circles) in the KOERI catalog with the solutions obtained for this study (yellow circles) by including MONGAN-1 network. Thin lines represent differences in the solutions for the same earthquakes. The blank and white filled triangles show the national network and the Ganos Fault monitoring network (MONGAN-1) stations used in the locations, respectively and b) a comparison of earthquake magnitudes (M_L) in the KOERI catalog with the magnitudes obtained in this study by including MONGAN-1 network. The orange line represents 1:1 harmony.

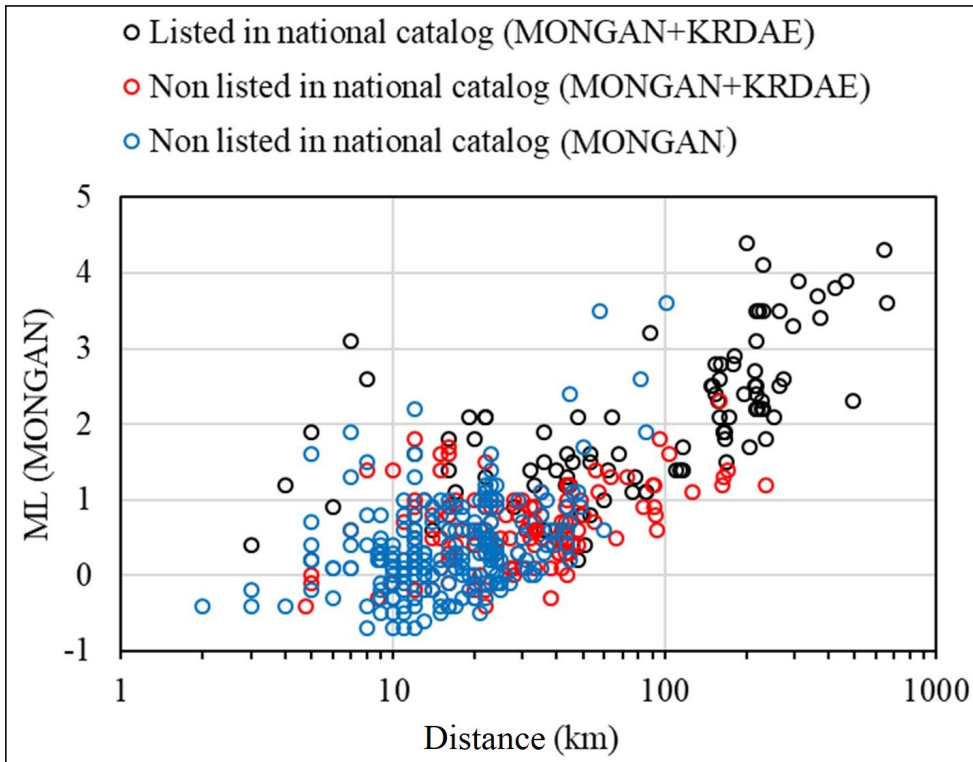


Figure 7- Magnitude-distance relationship of earthquakes obtained in this study for the three different groups.

groups. In Figure 8, the P wave delays at the stations for two examples of earthquakes occurring outside the network are shown with reference to the ATY station where the waves first arrived. As can be seen from the figure, the arrivals of P waves to the stations located in the north of the fault are significantly earlier than those in the south.

These early arrivals at the stations on the northern block cause a significant northward shift of the epicenters, especially when only MONGAN-1 seismograms are used. This is the reason why the epicenters represented by blue circles and partially red circles in Figure 5, unexpectedly emerge north of the main fault where no fault structure and no seismic activity in the national catalogs.

5. Analysis of Fault Zone Head Waves

In bimaterial fault blocks, FZHWs are observed at stations on the slow block, in addition to the early phase arrivals observed at stations on the fast block as exemplified above. These waves propagate along the interface using the fast block and reach the stations on the slow block (Figure 9). FZHW carries important

information about the fault zone to seismic stations (Ben-Zion and Aki, 1990). While the P wave directly reaching the station on the slow block from the source has a sharp initial (impulsive) form in the records, the FZHW reaching the station by refracting along the fault zone has a soft onset (emergent) form. FZHW spending a part of its journey in the fast block reaches before the direct P wave to the station located on the slow block of the fault and had a perpendicular distance to the fault $x < x_c$ (Figure 9);

$$x_c = r * \tan \left[\cos^{-1} \left(\frac{\alpha_2}{\alpha_1} \right) \right] \quad (2)$$

where x_c : critical distance from the fault, r : wave propagation distance along the fault, α_1 and α_2 represent fast and slow block velocities, respectively. The time difference (Δt) between the FZHW and the direct incident wave depends on the travel distance of the FZHW in the fault zone and the velocity difference between the blocks.

$$\Delta t \sim r \left[\left(\frac{1}{\alpha_2} \right) - \left(\frac{1}{\alpha_1} \right) \right] \quad (3)$$

FZHW and direct P waves have opposite polarities in earthquakes occurring close to the fault zone

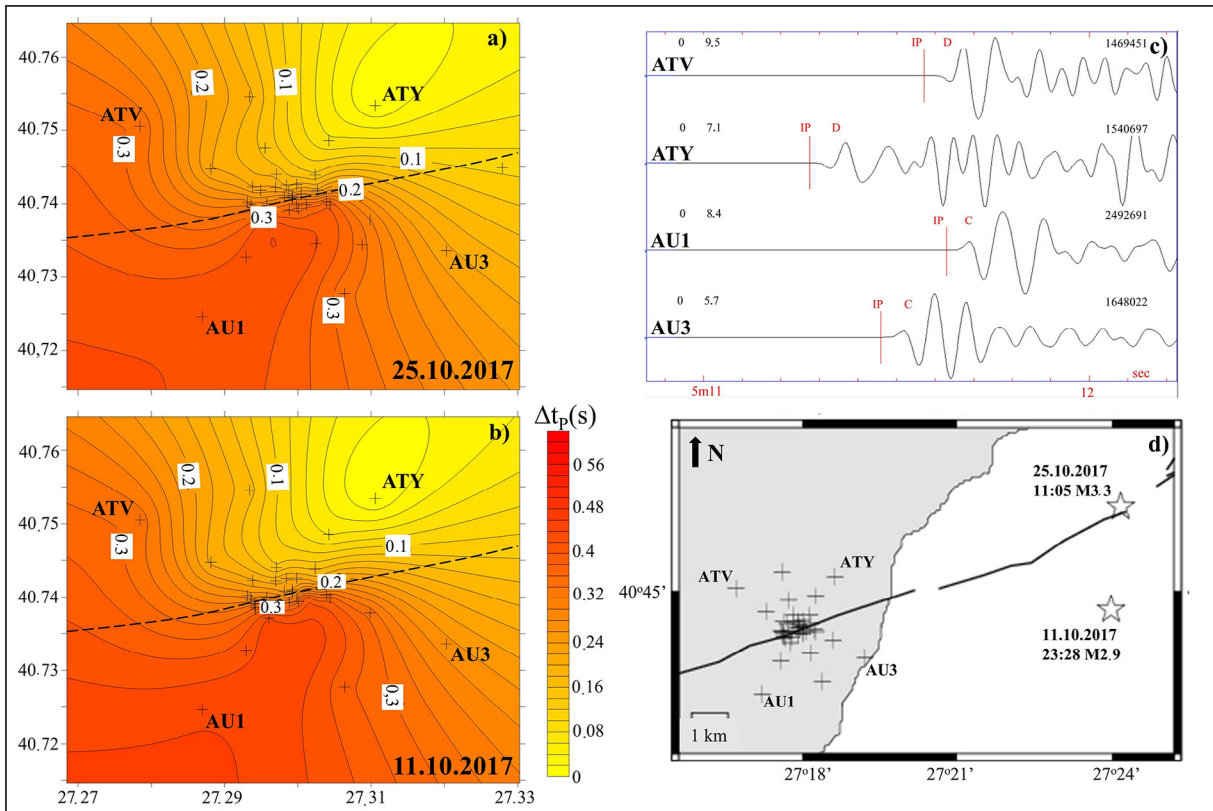


Figure 8- a), b) Contour maps of P wave delay times at network stations for two sample earthquakes (25.10.2017 and 11.10.2017) located in the east of MONGAN-1 network. Cross symbols and dashed lines indicate network station locations and the Ganos Fault, respectively. The delay times are normalized according to the arrival time of the first station (for both earthquakes at ATY station), c) P wave arrivals at sample stations for the 25 October 2017 earthquake marked with red lines and d) locations of the earthquakes (stars) and network stations (crosses).

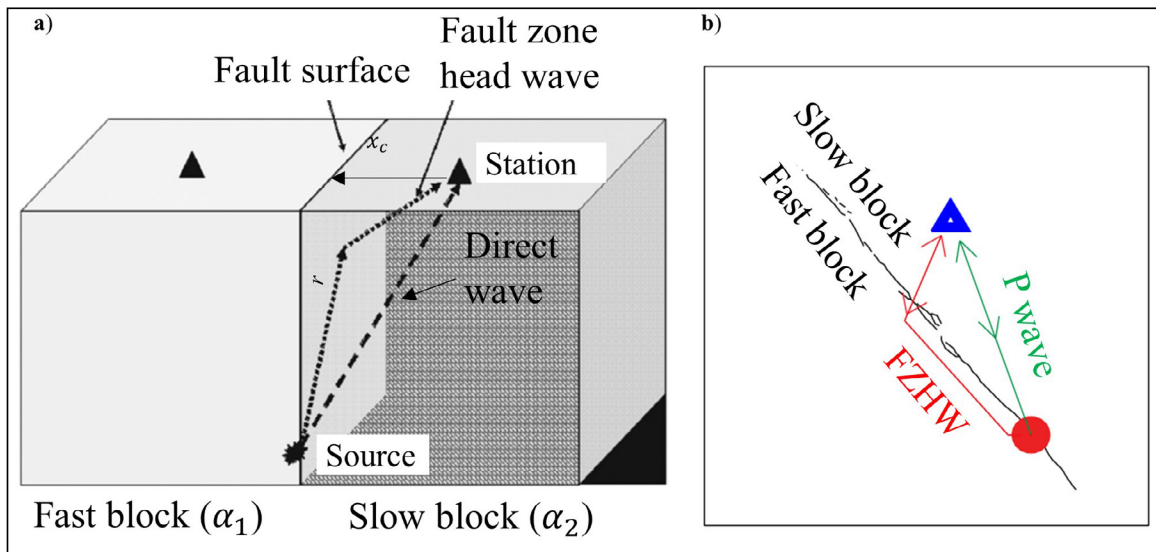


Figure 9- Schematic representation of the wave paths of fault zone head wave (FZHW) and direct P waves; a) Bennington et al. (2013) and b) Allam et al. (2014) have been modified.

(Ben-Zion, 1989, 1990). Another difference between these waves is the particle motion direction in the horizontal medium. While the particle motion is in the direction of the source in the direct incoming wave, this orientation is towards the fault zone in the FZHW (Bulut et al., 2012).

FZHW and direct P wave discrimination on the waveforms at stations close to the fault zone are generated by controlling for these differences. Software developed by Ross and Ben-Zion (2014) was used in the analysis, and the process flow chart is shown in Figure 10a. The program determines the first arrival time of the seismic motion in the vertical component using the STA/LTA ratios. Then, the arrival of a second wave phase is checked by using the Kurtosis and Skewness functions (Saragiotis et al., 2002). After determining these wave arrivals, their polarity is checked by looking at the particle motion of the waves. If the polarity direction of both waves is the same, no FZBD separation is made and the first arrival is directly marked as P wave. If these waves have opposite polarity with respect to each other, the first phase is marked as FZHW, and the following phase is marked as a direct P wave. Figure 10b indicates

the discrimination of FZHW and direct P waves in a sample earthquake seismogram. While the STA/LTA ratio marks the first wave phase, the second wave phase arrival in the Kurtosis function is very sharp. In the skewness function, the polarity transformation between the first and second wave phases occurs.

In this study, 68 earthquakes between October 2017 and May 2018 recorded by MONGAN-1 network stations were analyzed. As a result of this analysis, FZHW was found in 25 earthquake records. In Figure 11, analyzed and FZHW-detected earthquakes are shown in different colors.

As can be seen, the locations of the analyzed earthquakes are generally distributed in the extension of the fault in the Marmara Sea. FZHW detected earthquakes scattered among the others. While some of them are directly along the fault zone, the others are located in south of the fault zone. A distinctive feature related to the locations, magnitudes, and depths of earthquakes with and without FZHW could not be found for the analyzed dataset. In the continuation of the study, it was investigated which stations had more FZHW and which ones were not (Figure 12).

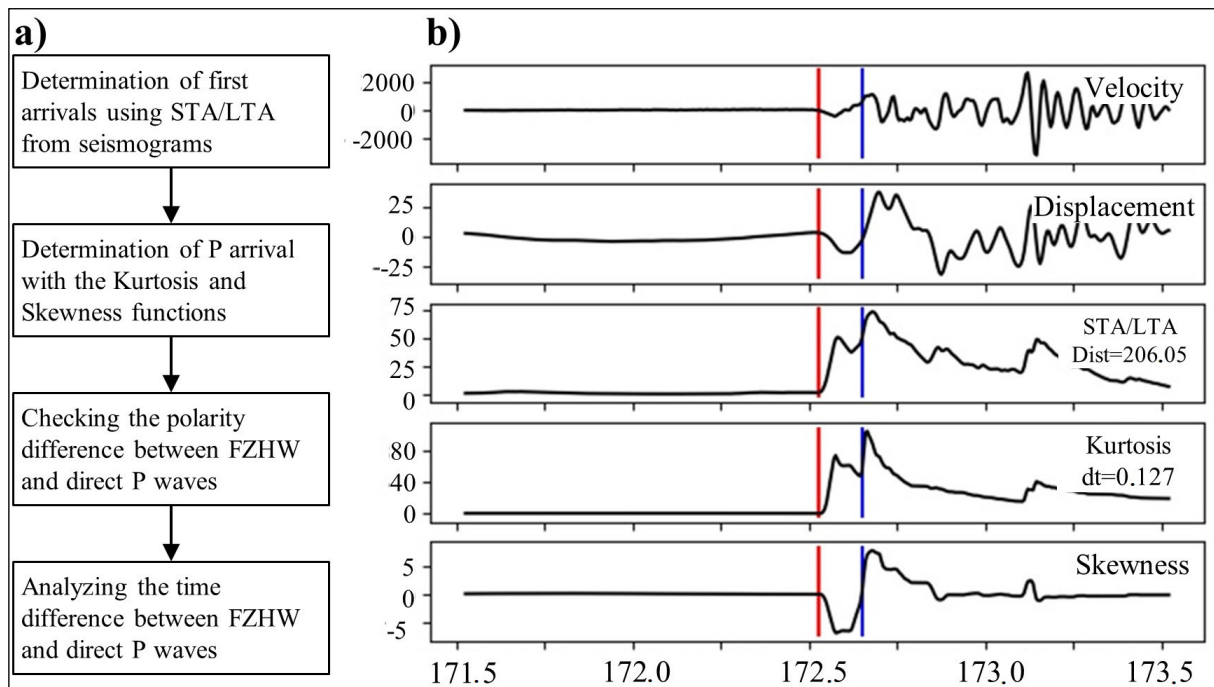


Figure 10- a) Processing steps in determining the fault zone head wave (FZHW) and b) markings of the P wave (blue line) and FZHW (red line) arrivals directly on a sample earthquake seismogram with the help of short time average/long time average (STA/LTA), Kurtosis and Skewness functions.

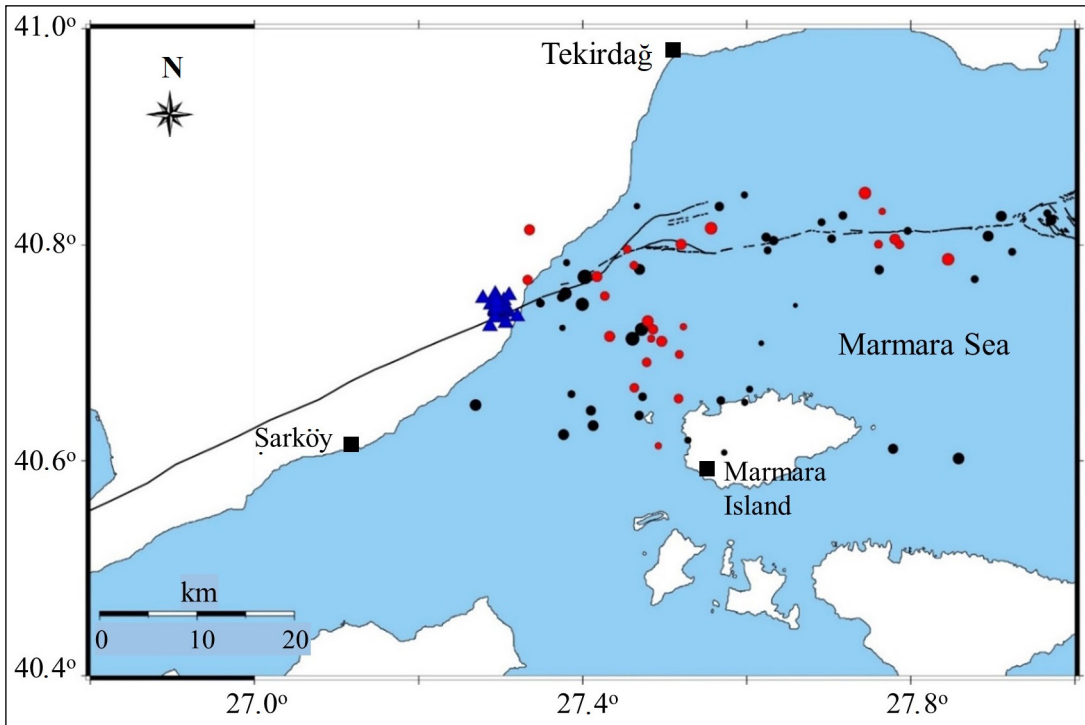


Figure 11- Locations of the analyzed earthquakes. Earthquakes with a fault zone head wave (FZHW) are shown by a red circle and earthquakes without an FZHW are represented by a black circle. The recording stations are indicated by blue triangles.

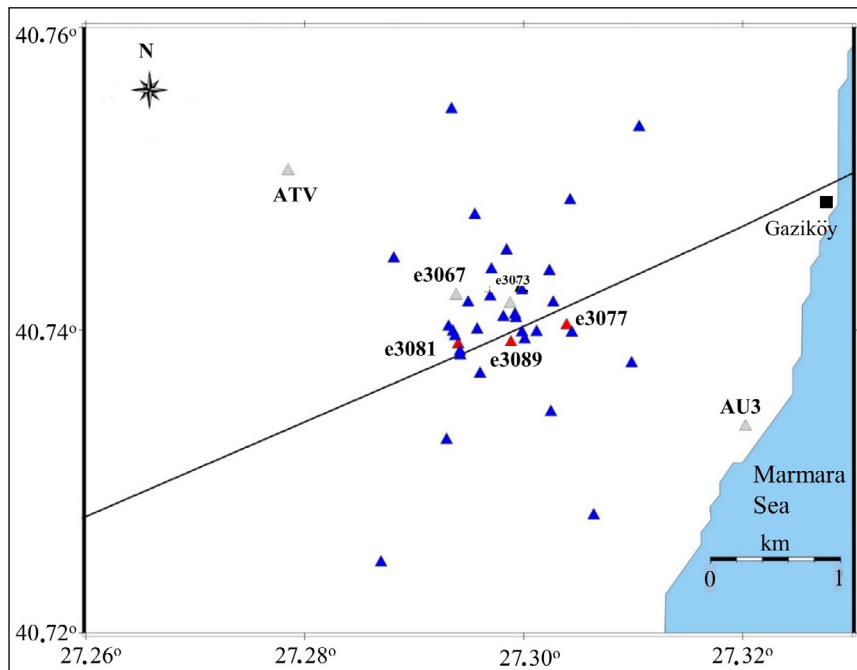


Figure 12- Distribution of stations for 25 earthquakes with fault zone head waves (FZHW). Seismic stations indicated by the red triangle recorded the highest number of FZHW. Seismic stations shown by gray triangles display none of FZHW.

As a result of this research, 36% of 25 earthquakes are observed at e3077, e3081 and e3089 stations. No FZHW could be obtained at ATW, AU3, e3067, and e3073 stations. Theoretically, FZHWs should be recorded at stations on the slow block. However, the analysis shows that FZHWs can be seen on both sides of the fault. Moreover, FZHW is observed in one of the two stations located on the slow side of the fault and very close to each other. According to our analysis, this case is common in stations with low signal-to-noise ratios.

6. Source Mechanism Solutions

The general feature of MONGAN network is that it detects small-magnitude earthquakes with large azimuthal gaps. In contrast, the signal-to-noise ratios are relatively high. In order to understand the stress conditions in the region, it is important obtaining reliable source mechanism solutions of these earthquakes. Since the moment tensor analysis method uses the entire waveform, it enables source mechanism solutions of small earthquakes with a small number of records (Fojtiková et al., 2010).

In this study, the ISOLA program developed by Sokos and Zahradnik (2008) was used for moment tensor analysis. ISOLA seismic moment tensor analysis is similar to Kikuchi and Kanamori (1991)'s multi-point source and iterative deconvolution method, but it uses the entire waveform differently. The inversion process starts with the calculation of Green's functions using the discrete wavenumber method defined by Bouchon (1981) for the displacement seismogram at each station, and the process is performed using the iterative deconvolution method. In the inversion process, synthetic seismograms are created in accordance with the initial parameters. Synthetic and observational seismograms are approximated to each other and the source mechanisms of earthquakes are tried to be determined. Since the method is based on a multi-source definition, a separate solution is generated for each source. Solutions with the smallest difference and the highest correlation between observational and

synthetic seismograms are preferred. The agreement between the observational and synthetic seismograms is measured by variance reduction (VR). In selecting the two most accurate double couple (DC) models representing the source mechanism, the variance values as well as the DC component ratio are taken into account.

As input parameters to the program; three components of each station's earthquake record in SAC (Seismic Analysis Code) format, crustal model information, earthquake occurrence time, magnitude and latitude, longitude information, and the duration of the earthquake are entered. In this study, different crustal models were tested and Yamamoto et al. (2015)'s crustal model was used. Figure 13 shows the moment tensor analysis of the $M_w=1.8$ earthquake that occurred on October 3, 2017, at 04:38 (GMT). In the analysis, recordings of at least 3 stations with a high signal-to-noise ratio are used. The analyzes are repeated in different frequency ranges from 0.5 Hz to 4 Hz, and the obtained values are compared. The time forms of the 1.6-3.3 Hz frequency range, where the best fit is achieved, are shown in Figure 13. As can be seen, synthetic observational fit (VR) > 0.40, Condition Number (CN) < 10, Source Mechanism Variation Index (FMVAR) < 30, and Spatial-Time Variation Index (STVAR) < 0.3 values indicate the success of the solution.

In Figure 14, the moment tensor solutions of 5 earthquakes with moment magnitudes $2.9 \leq M_w \leq 3.7$ are compared with the source mechanism solutions obtained with the zSacWin program (Yilmazer, 2003) using the first P wave polarities. While moment tensor solutions are calculated using MONGAN network seismograms with stations at a very narrow azimuth, first motion P wave polarities are calculated using national network station recordings surrounding the source. As can be seen, the solutions of both methods are quite similar. This result indicates that the moment tensor solutions obtained using a limited number of station coverage are reliable.

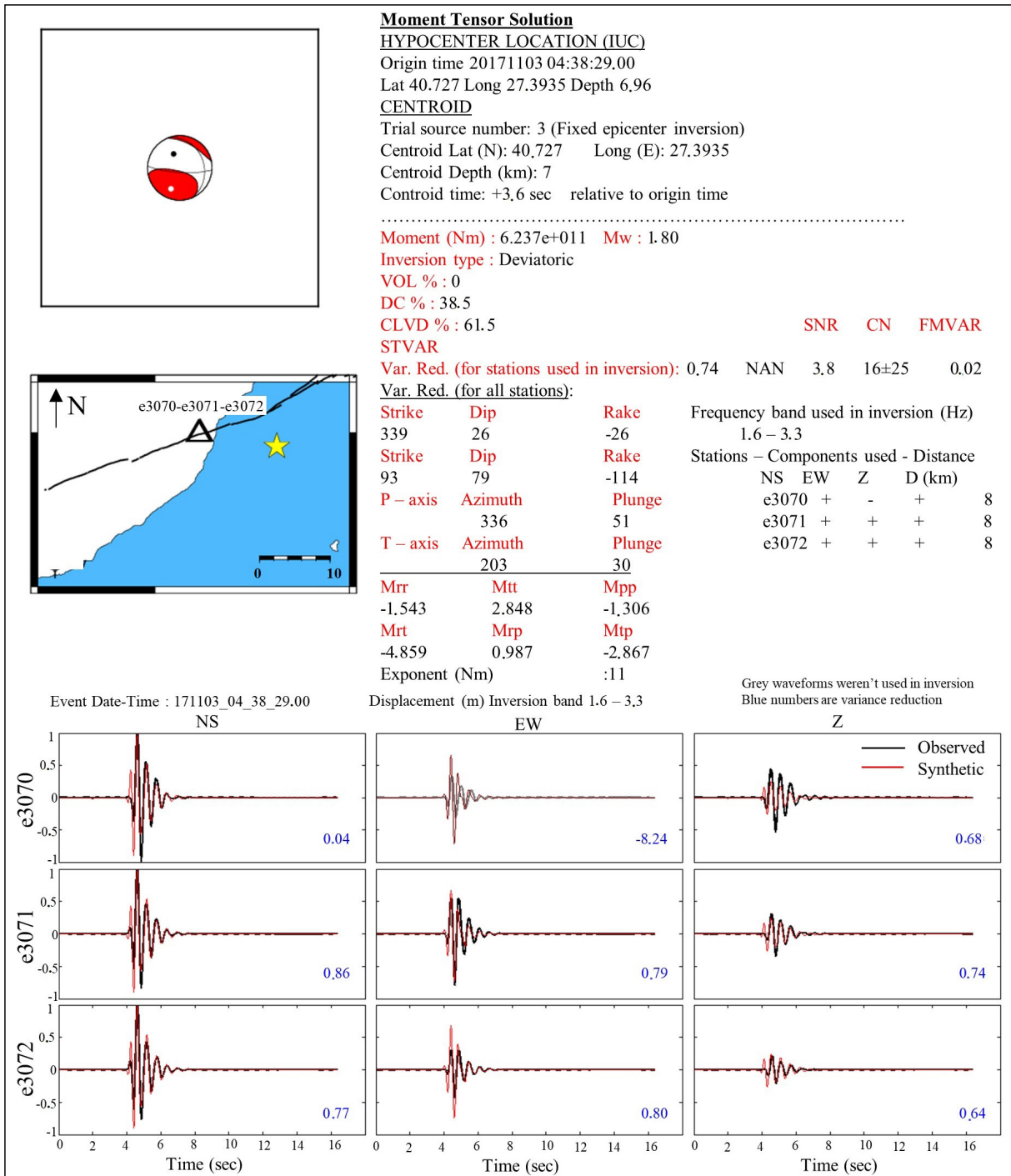


Figure 13- Moment tensor solution obtained by three station seismograms for the $M_w=1.8$ earthquake that occurred on 03.11.2017 at 04:38 (GMT). While the upper figure shows the solution parameters, the lower figure indicates the synthetic-observed waveform fitting.

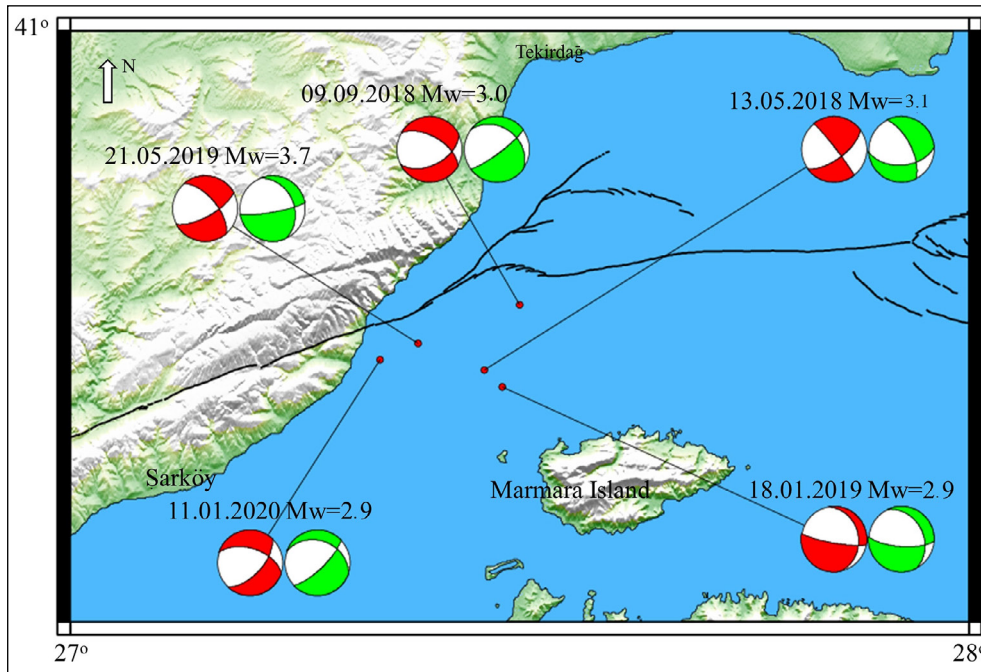


Figure 14- Comparison of source mechanisms obtained from first motion P wave polarity (green) with moment tensor analysis (red).

7. Results

MONGAN network data presents significant challenges and opportunities for earthquake detection, location and magnitude calculations, source mechanism solutions, and fault zone head wave detections. Reliable analyzes from the obtained data can make important contributions to the determination of the current seismicity of the Ganos Fault, the investigation of the fault zone structure, and the understanding of the local stress conditions. This study, which can be considered as a test analysis, has provided the opportunity to see the success limits of the applied analyzes and the necessity of alternative applications.

In the earthquake detection process from continuous data, there were 40%-50% differences between the STA/LTA method and manual check. The method is not achieved in sufficient success, especially in the detection of micro-earthquakes, due to low signal-to-noise ratios. By using different filters during the manual check, the simultaneous view of multiple station records is allowed us to observe microearthquakes. Since the manual check is a very laborious and time-consuming way, it is aimed to use

cross-correlation methods in the future stages of the study, especially in the detection of microearthquakes.

The presence of a sufficient number of stations surrounding the source region in earthquake analyses is very important in terms of increasing the quality of the location. Since MONGAN-1 network data is established in a very small area, it has large azimuthal gaps and produces high vertical/horizontal errors. At the same time, as a result of the very small distances between the stations, there is no difference between the observed wave arrivals in sufficient sensitivity. In addition, the fact that the stations are located on two different fault blocks, fast and slow, cause the waves to reach the stations on the fast block earlier than the stations on the slow block. All these reasons reduce the quality of earthquake solutions. On the other hand, there are many earthquakes that are not included in the national earthquake catalog and are recorded only by the MONGAN-1 network. These earthquakes are generally with $M < 1$ magnitude and are very local earthquakes. In order to increase the solution quality of these earthquakes, it seems essential to use different network techniques, such as beamforming, F-K, or including the source-azimuth directions to be obtained from the P wave first motion polarities (Havskov and

Ottmoller, 2010). In addition, it is expected that the calculation of the regional 3D velocity model and its inclusion in the event locations will increase the quality of the solution.

The effects of the bimaterial structure of the Ganos Fault zone are clearly observed in the seismic wave phases. While early phase arrivals are observed on the fast block in the north of the fault, FZHW arrivals are observed at the stations on the southern block. A systematic distinction regarding FZHW has not been revealed yet. When the number of discovering FZHW increases, the relationship between FZHW arrivals and structural elements can be established.

The results obtained regarding the moment tensor solutions of small earthquakes are remarkably promising. A comparison of different methods in the sample solutions shows that reliable source mechanism solutions can be obtained even with limited data which have a high signal-to-noise ratio. Using high-resolution crustal velocity models and high-frequency intervals are extremely important in testing microearthquakes by using small number of station recordings.

Acknowledgements

We would like to thank Patricia Martinez GARZON, Virgine DURAND, Amandine AMEMOUTOU, Felix KASTNER for their valuable contributions during the establishment of the MONGAN network. Moreover, we are also thankful to Mr. Sevim AVCI, Tekirdağ Metropolitan Municipality, and Dr. Murat NURLU, AFAD Presidency and Head of Earthquake Department who provide precious support to the field studies. This work is supported by TÜBİTAK-BMBF bilateral cooperation project number 118R019.

References

Aksoy, M. E., Meghraoui, M., Vallée, M., Çakır, Z. 2010. Rupture characteristics of the AD 1912 Mürefte (Ganos) earthquake segment of the North Anatolian Fault (western Turkey). *Geology* 38(11), 991-994.

Aksoy, M. E. 2021. The 9 August 1912 Mürefte-Şarköy earthquake of the North Anatolian fault. *Mediterranean Geoscience Reviews* 3, 95–114.

Allam, A. A., Ben-Zion, Y., Peng, Z. 2014. Seismic imaging of a bimaterial interface along the Hayward Fault, CA, with fault zone head waves and direct P arrivals. *Pure and Applied Geophysics* 171, 2993-3011.

Allen, R. 1978. Automatic earthquake recognition and timing from single traces. *Bulletin of the Seismological Society of America* 68, 1521-1532.

Andrews, D. J., Ben-Zion, Y. 1997. Wrinkle-like slip pulse on a fault between different materials. *Journal of Geophysical Research* 102, 553–571.

Armijo, R., Pondard, N., Meyer, B., Uçarkus, G., Mercier de Lépinay, B., Malavieille, J., Dominguez, S., Gutscher, M-A., Schmidt, S., Beck, C., Cagatay, N., Cakir, Z., Imren, C., Eris, K., Natalin, B., Özalaybey, S., Tolun, L., Lefèvre, I., Seeber, L., Gasperini, L., Rangin, C., Emre, O., Sarikavak, K. 2005. Submarine fault scarps in the Sea of Marmara pull-apart (North Anatolian Fault): implications for seismic hazard in Istanbul. *Geochemistry, Geophysics, Geosystems, AGU and the Geochemical Society* 6, Q06009.

Ben-Zion, Y. 1989. The response of two joined quarter spaces to SH line sources located at the material discontinuity interface. *Geophysical Journal International* 98, 213–222.

Ben-Zion, Y. 1990. The response of two half spaces to point dislocations at the material interface. *Geophysical Journal International* 101, 507–528.

Ben-Zion, Y., Aki, K. 1990. Seismic radiation from an SH line source in a laterally heterogeneous planar fault zone. *Bulletin of the Seismological Society of America* 80(4), 971-994.

Ben-Zion, Y., Malin, P. 1991. San Andreas fault zone head waves near Parkfield, California. *Science* 251, 1592–1594.

Bennington, N. L., Thurber, C., Peng, Z., Zhang H., Zhao P. 2013. Incorporating fault zone head wave and direct wave secondary arrival times into seismic tomography: Application at Parkfield, California. *Journal of Geophysical Research: Solid Earth* 118, 1008-1014.

Bentz, S., Martínez-Garzón, P., Kwiatek, G., Dresen, G., Bohnhoff, M. 2019. Analysis of microseismicity framing $M_L > 2.5$ earthquakes at the Geysers geothermal field, California. *Journal of Geophysical Research: Solid Earth* 124, 8823–8843.

- Bohnhoff, M., Bulut, F., Dresen, G., Malin, P. E., Eken, T., Aktar, M. 2013. An earthquake gap south of İstanbul. *Nature Communication* 4, 1999.
- Bohnhoff, M., Martínez-Garzón, P., Bulut, F., Stierle, E., Ben-Zion, Y. 2016. Maximum earthquake magnitudes along different sections of the North Anatolian fault zone. *Tectonophysics* 674, 147–165.
- Bohnhoff, M., Wollin, C., Domigall, D., Küperkoch, L., Martínez-Garzón, P., Kwiatek, G., Dresen, G., Malin, P. E. 2017. Repeating Marmara Sea earthquakes: indication for fault creep. *Geophysical Journal International* 210(1), 332–339.
- Bouchon, M. 1981. A simple method to calculate Green's functions for elastic layered media. *Bulletin of the Seismological Society of America* 71(4), 959–971.
- Bulut, F., Ben-Zion, Y., Bohnhoff, M. 2012. Evidence for a bimaterial interface along the Mudurnu segment of the North Anatolian fault zone from polarization analysis of P waves. *Earth and Planetary Science Letters* 327, 17–22.
- Bulut, F., Aktuğ, B., Yaltrak, C., Doğru, A., Özener, H. 2019. Magnitudes of future large earthquakes near İstanbul quantified from 1500 years of historical earthquakes, present-day microseismicity and GPS slip rates. *Tectonophysics* 764, 77-87.
- Ergintav, S., Reilinger, R. E., Çakmak, R., Floyd, M., Cakir, Z., Doğan, U., King, R. W., McClusky, S., Özener, H. 2014. İstanbul's earthquake hot spots: Geodetic constraints on strain accumulation along faults in the Marmara seismic gap. *Geophysical Research Letters* 41, 5783– 5788.
- Fojtiková, L., Vavryák, V., Cipciar, A., Madarás, J. 2010. Focal mechanisms of micro-earthquakes in the Dobrá Voda seismoactive area in the Malé Karpaty Mts. (Little Carpathians), Slovakia. *Tectonophysics* 492(1-4), 213-229.
- Gibbons, S. J., Ringdal, F. 2006. The detection of low magnitude seismic events using array-based waveform correlation. *Geophysical Journal International* 165, 149–166.
- Havskov, J., Ottemoller, L. 1999. SeisAn Earthquake Analysis Software. *Seismological Research Letters* 70, 532–534.
- Havskov, J., Ottemoller L. 2010. *Routine Data Processing in Earthquake Seismology*. Springer, 347.
- Kalafat, D., Gürbüz, C., Üçer, S. B. 1987. Batı Türkiye'de kabuk ve üst manto yapısının araştırılması. *Deprem Araştırma Bülteni* 59, 43-64.
- Kikuchi, M., Kanamori, H. 1991. Inversion of complex body waves. III. *Bulletin of the Seismological Society of America* 81, 2335–2350.
- Lange, D., Kopp, H., Royer, J.Y., Henry, P., Çakir, Z., Petersen, F., Sakic, P., Ballu, V., Bialas, J., Özeren, M. S., Ergintav, S., Géli, L. 2019. Interseismic strain build-up on the submarine North Anatolian Fault offshore İstanbul. *Nature Communications* 10(1), 3006.
- Li, Y. G., Leary, P. C. 1990. Fault zone trapped seismic waves. *Bulletin of the Seismological Society of America* 80(5), 1245-1271.
- Lienert, B. R., Havskov, J. 1995. A computer program for locating earthquakes both locally and globally. *Seismological Research Letters* 66(5), 26-36.
- Mcclusky, S., Balassanian, S., Barka, A., Demir, C., Ergintav, S., Georgiev, I., Gurkan, O., Hamburger, M., Hurst, K., Kahle, H.G., Kastens, K., Kekelidze, G., King, R., Kotzev, V., Lenk, O., Mahmoud, S., Mishin, A., Nadariya, M., Ouzounis, A., Veis, G. 2000. Global positioning system constraints on plate kinematics and dynamics in the eastern Mediterranean and Caucasus. *Journal of Geophysical Research* 105, 5695-5719.
- McGuire, J., Ben-Zion, Y. 2005. High-resolution imaging of the bear valley section of the San Andreas fault at seismogenic depths with fault zone head waves and relocated seismicity. *Geophysical Journal International* 163, 152–164.
- Okay, A., Özcan, E., Cavazza, W., Okay, N., Less, G. 2010. Basement types, Lower Eocene aeries, Upper Eocene Olistostromes and the initiation of the Southern Thrace Basin, NW Turkey. *Turkish Journal of Earth Sciences* 19, 1–25.
- Özalaybey, S. 2010. Marmara Denizi'nde depremsellik gözlem altyapı kapasitesinin güncellenmesi sonuç raporu. TÜBİTAK, Proje No: CAYDAG-105Y369.
- Ross, Z. E., Ben-Zion, Y. 2014. Automatic picking of direct P, S seismic phases and fault zone head waves. *Geophysical Journal International* 199(1), 268-381.
- Sakic, P., Piété, H., Ballu, V., Royer, J. Y., Kopp, H., Lange, D., Petersen, F., Özeren, M. S., Ergintav, S., Geli, L., Henry, P., Deschamps, A. 2016. No significant

- steady state surface creep along the North Anatolian Fault offshore İstanbul: results of 6 months of seafloor acoustic ranging. *Geophysical Research Letters* 43(13), 6817–6825.
- Saragiotis, C., Hadjileontiadis, L., Panas, S. 2002. PAI-S/K: a robust automatic seismic P phase arrival identification scheme. *IEEE Transactions on Geoscience and Remote Sensing* 40, 1395–1404.
- Schmittbuhl, J., Karabulut, H., Lengliné, O., Bouchon, M. 2016. Seismicity distribution and locking depth along the main Marmara Fault. *Turkish Geochemistry, Geophysics, Geosystems* 17, 954–965.
- Sokos, E., Zahradník, J. 2008. ISOLA- A Fortran code and Matlab GUI to perform multiple point source inversion of seismic data. *Computers and Geosciences* 34, 967–977.
- Stein, R. S., Barka, A. A., Dieterich, J. H. 1997. Progressive failure on the North Anatolian fault since 1939 by earthquake stress triggering. *Geophysical Journal International* 128, 594–604.
- Uchida, N., Kalafat, D., Pınar, A., Yamamoto, Y. 2019. Repeating earthquakes and interplate coupling along the western part of the North Anatolian Fault. *Tectonophysics* 769, 228185.
- Uçarkuş, G., Çakır, Z., Armijo, R. 2011. Western termination of the Mw 7.4, 1999 İzmit earthquake rupture: Implications for the expected large earthquake in the Sea of Marmara. *Turkish Journal of Earth Sciences* 20, 379–394.
- Wollin, C., Bohnhoff, M., Martínez-Garzón, P., Küperkoch, L., Raub, C. 2018. A unified earthquake catalogue for the Sea of Marmara Region, Turkey, based on automatized phase picking and travel-time inversion: seismotectonic implications. *Tectonophysics* 747-748, 416-444.
- Yalçınkaya, E., Bohnhoff, M., Görgün, E., Alp, H., Bentz, S., Pınar, A., Alver, F., Kılıçarslan, Ö., Tamtaş, B.D., Görgün, B. 2022. Ganos fayı güncel deprem etkinliğinin değerlendirilmesi: MONGAN sismik ağ yapısı ve veri kalitesi. *Hacettepe Yerilimleri Dergisi* 43(1), 37-60.
- Yılmaz, M. 2003. Deprem kaynak parametrelerinin online belirlenmesi, Yüksek Lisans Tezi, İstanbul Üniversitesi, Fen Bilimleri Enstitüsü, Jeofizik Mühendisliği Ana Bilim Dalı, İstanbul, 57.
- Yamamoto, Y., Takahashi, N., Çıtak, S., Kalafat, D., Pınar, A., Gürbüz, C., Kaneda, Y. 2015. Offshore seismicity in the western Marmara Sea, Turkey, revealed by ocean bottom observation. *Earth Planets Space* 67, 147.
- Yamamoto, Y., Takahashi, N., Pınar, A., Kalafat, A., Çıtak, S., Comoğlu, M., Polat, R., Kaneda, Y. 2017. Geometry and segmentation of the North Anatolian Fault beneath the Marmara Sea, Turkey, deduced from long-term ocean bottom seismographic observations. *Journal of Geophysical Research: Solid Earth* 122.
- Yamamoto, R., Kido, M., Ohta, Y., Takahashi, N., Yamamoto, Y., Pınar, A., Kalafat, D., Özener, H., Kaneda, Y. 2019. Seafloor geodesy revealed partial creep of the North Anatolian Fault submerged in the sea of Marmara. *Geophysical Research Letters* 46(3), 1268–1275.
- Yamamoto, Y., Kalafat, D., Pınar, A., Takahashi, N., Polat, R., Kaneda, Y., Özener, H. 2022. Seismic velocity structure along the North Anatolian Fault beneath the Central Marmara Sea and its implication for seismogenesis. *Geophysical Journal International* 228(1), 396–411.
- Yoon, C. E., O'Reilly, O., Bergen, K. J., Beroza, G. C. 2015. Earthquake detection through computationally efficient similarity search. *Science Advances* 1, e1501057.